ISSN 0003-701X, Applied Solar Energy, 2023, Vol. 59, No. 5, pp. 595–603. © Allerton Press, Inc., 2023.

SOLAR ENGINEERING MATERIALS SCIENCE

Effect of the Sb/Se Ratio on the Structural and Electrical Properties of Sb_xSe_y Films

M. S. Tivanov[a], *, T. M. Razykov[b], K. M. Kuchkarov[b], D. S. Bayko[a], I. A. Kaputskaya[a], R. T. Yuldoshov[b], and M. P. Pirimmetov[b]

[a] *Faculty of Physics, Belarusian State University, Minsk, 220030 Belarus*

[b] *Physical-Technical Institute, Uzbekistan Academy of Sciences, Tashkent, 100084 Uzbekistan*

* *e-mail: tivanov@bsu.by*

Received June 14, 2023; revised October 12, 2023; accepted October 16, 2023

Abstract—Sb_xSe_y thin films were obtained from precursor of pure antimony and selenium granules evaporated in the temperature ranges from 980 to 1025°C for Sb and 415 to 470°C for Se by chemical molecular beam deposition method on glass substrates. It was found that the films consist mainly of the Sb_xSe_y phase and have a different Sb/Se ratio in the range from stoichiometry to 0.89. Controlling the fraction of components allows to change the orientation of crystallites, which, in turn, leads to changes in electrical conductivity.

Keywords: Antimony selenide (Sb_2Se_3), chemical molecular beam deposition (CMBD), Raman spectroscopy, surface morphology, X-ray diffraction, electrical properties

DOI: 10.3103/S0003701X23600959

INTRODUCTION

One of the most important aims of modern materials science is development of new inexpensive and efficient solar energy converters based on low toxic and widely spread chemical elements to replace currently used commercial photovoltaic converters based on Si, a-Si, CdTe, $Cu(In,Ga)(Se,S)_2$ [1].

Antimony selenide (Sb_2Se_3) is one of the most promising materials for use as the base layer of solar cells due to the following advantages: optimal band gap (1.1–1.3 eV), high absorption coefficient $>10^5$ cm^{-1}, *p*-type conductivity, high resistance to external influences, constituent chemical elements are earth-abundant, low-cost and non-toxic [2, 3]. According to published data, the following methods can be used to fabricate thin Sb_2Se_3 films: thermal evaporation in vacuum [4], vacuum evaporation [5], rapid thermal evaporation [6], magnetron sputtering [7], closed-space sublimation [8], electrochemical deposition [9], spin coating [10], aerosol-assisted chemical vapor deposition [11], vapor transport deposition [12]. The chemical molecular beam deposition (CMBD) [13] using here is potentially more preferable because this method allows to obtain various compositions of thin films by varying the synthesis time, the temperature of the substrate and sources, the flow rate of the carrier gas, does not require complex technical solutions such as maintaining a vacuum or using high-power laser radiation. However, to date, the effect of synthesis conditions by CMBD method on the properties and dynamics of changes in Sb_2Se_3 films has been poorly studied.

In this work, we study the dependence of the morphology, crystal structure and electrical properties of Sb_xSe_y films on the concentration ratio of Sb/Se components during synthesis by the CMBD method.

EXPERIMENTAL AND RESEARCH METHODS

Sb_xSe_y layers were deposited by CMBD method. A schematic representation of the CMBD method is shown in Fig. 1, this method is described in detail in [14, 15]. The process of producing Sb_xSe_y films by CMBD was as follows. The grenules of the Sb (antimony) and the Se (selenium) elements of semiconductor grade (99.999%) were used as initial material. The material of semiconductor grade sources was placed into the containers: Sb into one, and Se into the other. Then, the system was prepared for operation and was blown out by hydrogen to remove atmospheric contaminating gases. Next, the external furnace of the reaction chamber was switched on. The heating level was determined by the specified deposition temperatures that were controlled by thermocouples. As soon as the substrate was heated to a required level, the furnaces of individual heating of the Sb and the furnace for Se heating were switched on and were brought up to required evaporation temperatures. The temperature interval of evaporation of granules in the Sb and selenium for growing the films was within the range of 980 to 1025°C for Sb and 415 to 470°C for Se,

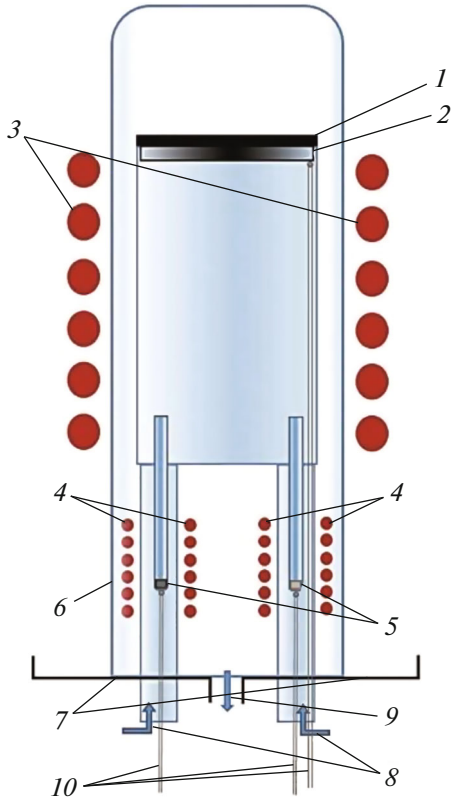

Fig. 1. Schematic representation of the CMBD method for obtaining Sb_xSe_y thin films. (*1*, *2*) holder and substrate, (*3*) substrate heater, (*4*) source heaters, (*5*) crucibles of evaporated components, (*6*) reactor cap, (*7*) flange, (*8*) gas inlet, (*9*) gas outlet, (*10*) thermocouples.

while the substrate temperature was maintained at 500°C. The flow of hydrogen carrier gas was ~20 cm^3/min. The duration of the deposition process depends on the required thickness of the films and equals 30 min. Soda-lime glass a size of 2 × 2 cm^2 were used as substrates. To fabricate Se-rich Sb_xSe_y films with a stoichiometric composition, we changed partial pressure of Se in the vapor phase during the process of their growth.

The elemental composition of the synthesized films was determined by X-ray spectral microanalysis using an energy-dispersive nitrogen-free spectrometer Aztec Energy Advanced X-Max 80 with an energy spectral resolution of 125 eV and a sensitivity for determining chemical elements of 0.2 at %. Particularities of the surface morphology were studied by scanning electron microscopy (SEM) using a LEO-1455 VP microscope (Carl Zeiss) in secondary electrons mode with accelerating voltage of 20 kV. The surface topography was studied using a scanning probe microscope SOLVER NANO in the semi-contact mode by a cantilever with a tip radius of 10 nm at a resonant frequency 236 kHz, the lateral resolution was better than 40 nm and the vertical resolution was better than 0.5 nm. X-ray diffraction patterns were recorded using Rigaku Ultima IV high-resolution diffractometer with a Cu Kα radiation wavelength 0.15418 nm scanned in the range of 10° to 60° with a step of 0.05°. Phase identification was carried out by comparing the experimentally determined interplanar distances with tabular values from the database of the Joint Committee for the Powder Diffraction Standard (JCPDS). The crystal lattice parameters (a, b, c) were determined using Rigaku Data Analysis Software PDXL2 (version 2.8.4.0) by the formulas:

— for Sb_2Se_3 belonging to the rhombic syngony

$$\frac{1}{d_{hkl}^2} = \left(\frac{h^2}{a^2} + \frac{k^2}{b^2} + \frac{l^2}{c^2}\right), \quad (1)$$

— for Sb belonging to the trigonal (rhombohedral) syngony

$$\frac{1}{d_{hkl}^2} = \frac{\left(h^2 + k^2 + l^2\right)\sin^2\phi + 2(hk + kl + hl)(\cos^2\phi - \cos\phi)}{a^2(1 - 3\cos^2\phi + 2\cos^3\phi)}, \quad (2)$$

where ϕ is the angle between the base vectors.

The Raman spectra were measured at room temperature using a Nanofinder HE (LOTIS TII) confocal spectrometer. A solid-state laser with a wavelength of 532 nm was used. Laser radiation with a power of 60 μW was focused on the surface of the samples to a region about 0.7 μm in diameter. The spectral resolution was no worse than 3 cm^{-1}.

To measure the resistance dependency on temperature, we used 3 × 5 mm^2 samples with silver paste contacts. The distance between the contacts was in the range of 0.4–0.7 mm. The dependences of the resistance on temperature were established by the two-probe method in the temperature range of 25–100°C in an evacuated cell with a residual pressure of p = 5 Pa. To measure the resistance of the sample, we used a direct current source-meter Keithley 2400, which makes it possible to measure currents in the range of 10^{-11}–1 A and voltages in the range of 10^{-6}–100 V with an accuracy of no worse than 0.1%. Lackeshore 332 temperature controller was used to regulate and control the temperature on the sample. The temperature was measured using a Pt-100M resistance thermometer fixed near the sample, which makes it possible to measure the temperature with an accuracy of ±0.3°C.

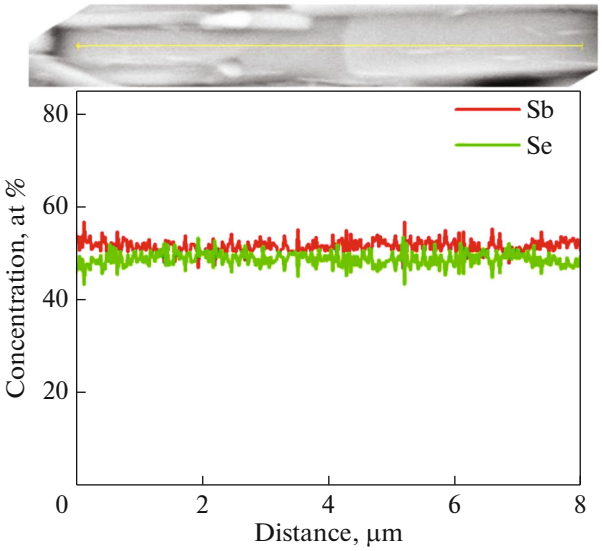

Fig. 2. Distribution of chemical elements along the scanning line for a sample with the ratio Sb/Se = 0.66.

RESULTS AND DISCUSSION

The percentage content of chemical elements in the synthesized films was determined by X-ray spectral microanalysis. It has been found that the films consist of selenium and antimony, and the distribution of Sb and Se along the scanning line over the surface is uniform (Fig. 2). Films with concentration ratios Sb/Se = 0.66, 0.72, 0.82, and 0.89 were obtained at source temperatures of 830–1000°C.

The surface morphology of the Sb_xSe_y films is shown in micrographs obtained using scanning electron microscopy (Fig. 3). As can be seen from Fig. 3, the films are formed from microcrystals in the form of rods, which, depending on the ratio of Sb/Se concentrations, have different sizes, arrangement density, and slope with respect to the substrate.

For the thin films with the ratio of Sb/Se concentrations equal to 0.66 and 0.72 a similar surface morphology is found, the length of the rods is 5–10 μm, and the diameter is 1–2 μm. However, for a film with Sb/Se = 0.66, rods grow preferentially parallel to the substrate, while for a film with Sb/Se = 0.72, they grow at an angle to the substrate, and the rods themselves are slightly larger. An increase in the content of Sb and a deviation from the stoichiometric ratio (samples with Sb/Se = 0.82 and 0.89) cause a change in the morphology of the film surface: the centers of microcrystal formation are distributed unevenly over the surface of the substrate, areas of accumulation of microcrystals clearly detected; the sizes of microcrystals become smaller (the length of the rods is 2–4 μm and the diameter is 0.5–1 μm). In this case, the growth of microcrystals without a preferential orientation with respect to the substrate is detected.

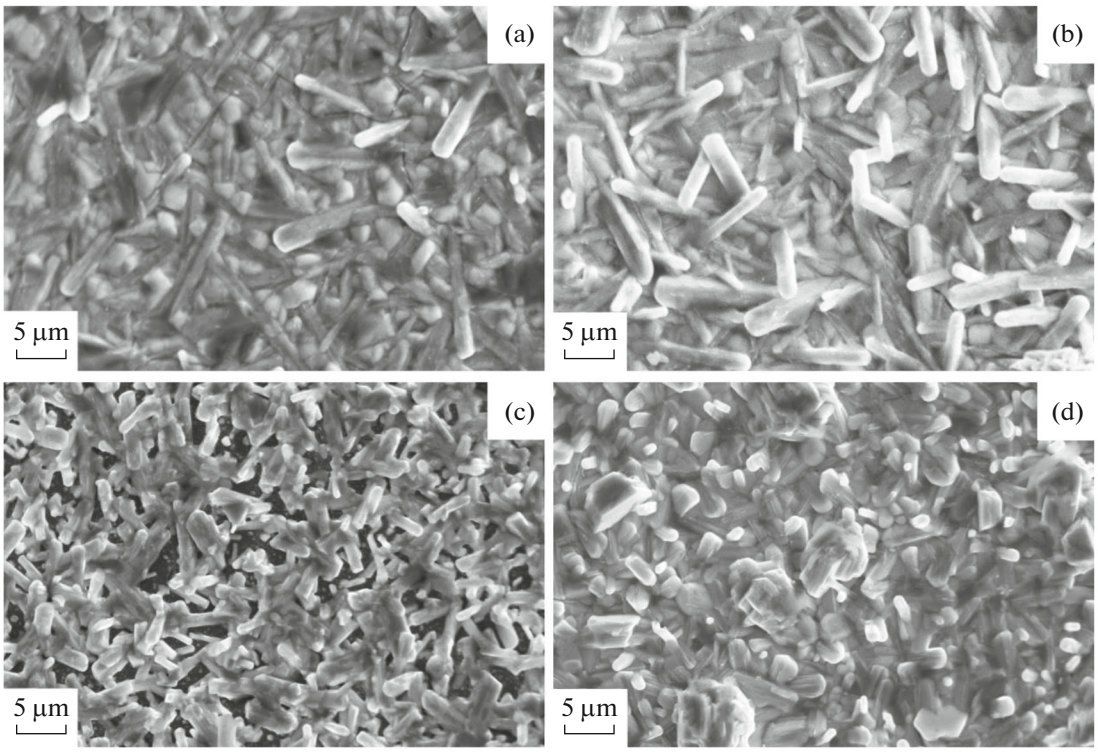

Fig. 3. SEM images of the surface of Sb_xSe_y thin films with the ratio Sb/Se concentrations 0.66 (a), 0.72 (b), 0.82 (c) and 0.89 (d).

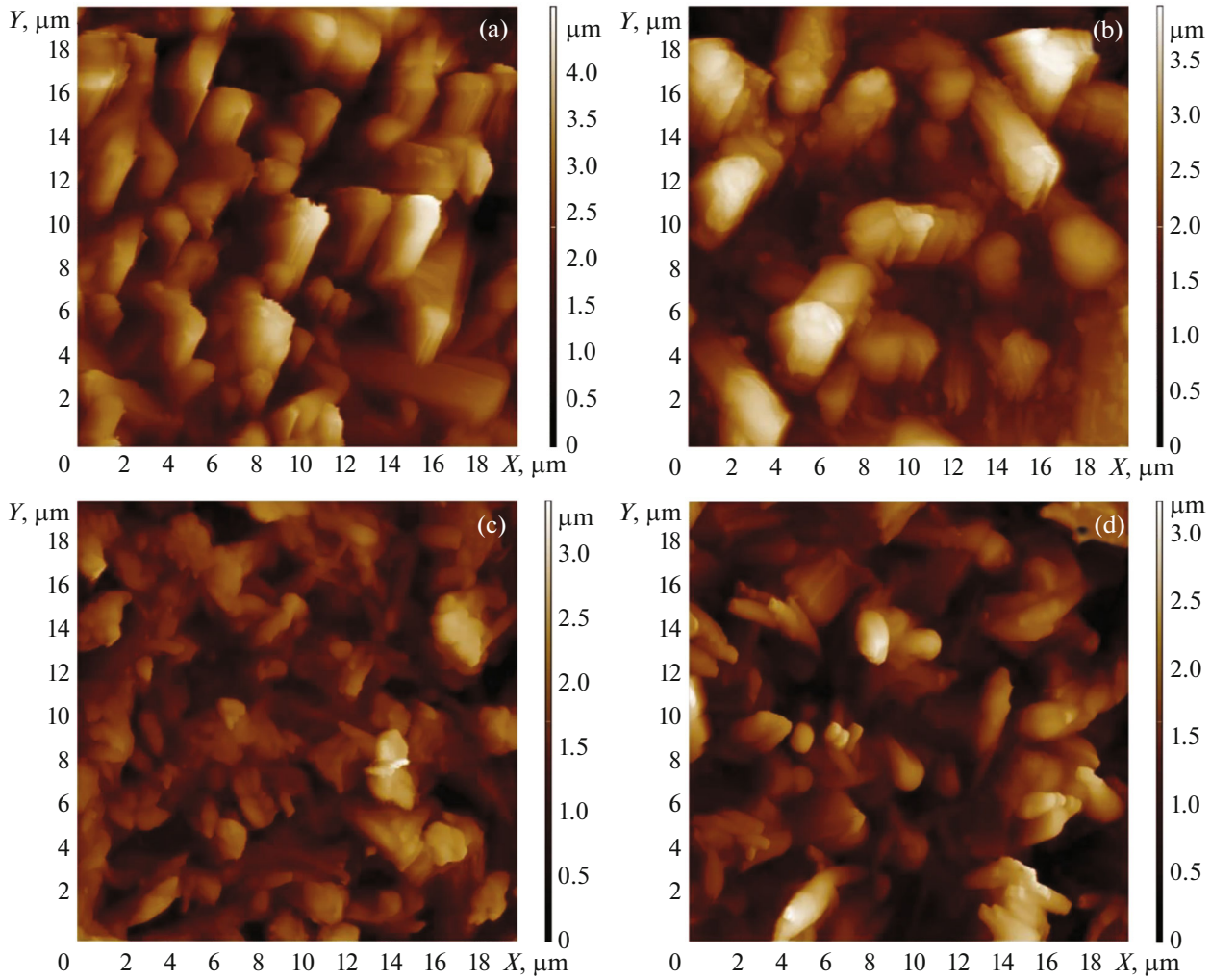

Fig. 4. AFM images of the surface of Sb_2Se_3 thin films with the ratio Sb/Se concentrations 0.66 (a), 0.72 (b), 0.82 (c) and 0.89 (d).

Figure 4 shows the topography of the film surface. The calculated roughness parameters are given in Table 1. The obtained films have a developed surface relief, the value of the root-mean-square (RMS) roughness is in the range 0.53–0.77 μm. In this case, films with Sb/Se = 0.82 have the smallest values of the roughness parameters Sa and Sq, while films with Sb/Se = 0.66 have the largest values. All films are characterized by a positive asymmetry in the distribution of surface heights (~0.4–0.6), indicating the predominance of high peaks in the surface relief [16].

Figure 5 shows X-ray diffraction patterns of the obtained samples of Sb_xSe_y films. The diffraction patterns show intense lines at $2\theta = 15.03°$, 16.87°, 24.15°, 27.39°, 28.20°, 31.16°, 32.22°, 34.07°, 35.70°, 44.95°, 51.88° corresponding to planes (020), (120), (310), (230), (211), (221), (301), (240), (321), (431), (061) Sb_2Se_3 phases according to JCPDS card 00-015-0861,

Table 1. Surface roughness parameters of Sb_xSe_y films synthesized with the different ratio Sb/Se

Sb/Se ratio	0.66	0.72	0.82	0.89
Average roughness Sa, μm	0.62	0.49	0.42	0.54
RMS roughness Sq, μm	0.76	0.62	0.53	0.67
Ssk asymmetry	0.55	0.39	0.41	0.64
Ska kurtosis	2.83	3.48	3.29	3.24

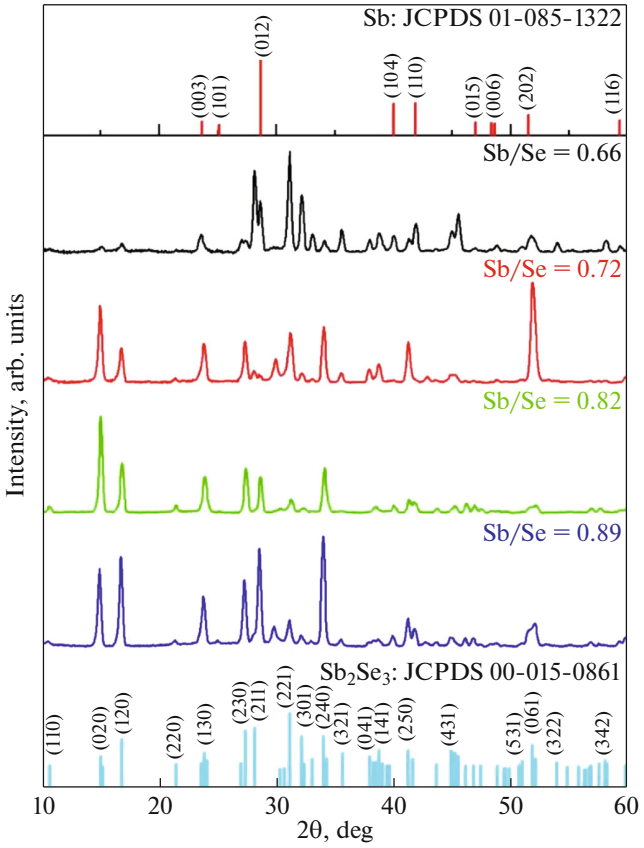

Fig. 5. XRD images of Sb_xSe_y thin films with the ratio Sb/Se concentrations 0.66 (a), 0.72 (b), 0.82 (c) and 0.89 (d).

and lines with smaller intensities at 2θ = 23.66°, 28.67°, 40.06°, 41.89°, 51.57°, 59.36° corresponding to planes (003), (012), (104), (110), (202), (024) of the Sb phase according to JCPDS card 01-085-1322. Thus, a qualitative phase analysis indicates that the obtained films consist mainly of Sb_2Se_3 and, to a lesser extent, of Sb, which corresponds to the state diagram of the Sb-Se system [17].

The integrated intensity of Sb reflections increases with increasing Sb/Se ratio, but the volume fraction of the Sb phase with respect to Sb_xSe_y remains small. In accordance with the JCPDS file index, the Sb_2Se_3 phase has a rhombic crystal structure (space group *Pnma*, no. 62), while the Sb phase has a trigonal crystal structure (space group *R-3m*, no. 166). Unit cell parameters of the Sb_2Se_3 and Sb phases, calculated by formulas (1) and (2) for different ratio Sb/Se concentrations, are shown in Fig. 6. Calculated parameters appeared to be similar to the tabular values: for Sb_2Se_3 $a = 1.1630$ nm, $b = 1.1780$ nm, $c = 0.3985$ nm (JCPDS 00-015-0861), for Sb $a = 0.4308$ nm, $b = 0.4308$ nm, $c = 1.1274$ nm (JCPDS 01-085-1322), no significant changes in the unit cell parameters with a change in the Sb/Se ratio were found.

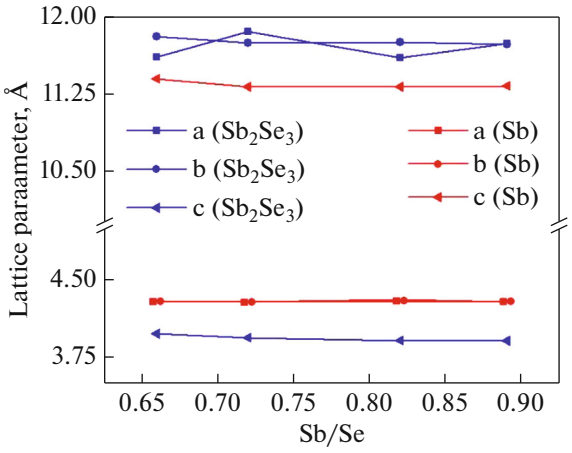

Fig. 6. Crystal lattice parameters of Sb_xSe_y and Sb phases.

To gain a deeper understanding of the dependence of the structural properties of samples on the Sb/Se ratio, we use the Scherrer's formula [18, 19], covering the contribution of grain size to peak broadening:

$$D = \frac{0.9\lambda}{\beta \cos \theta_{hkl}}, \quad (3)$$

where β is the FWHM, λ is the X-ray wavelength (0.15418 nm), D is the grain size, θ_{hkl} is the Bragg angle.

The calculated by the formula (3) values of D are in the range from a minimum of 217 nm for the ratio Sb/Se = 0.72 to a maximum of 233 nm for the stoichiometric ratio. It can be concluded that the grain size practically does not depend on the ratio of antimony and selenium in this films.

Sb_xSe_y films were additionally analyzed by Raman spectroscopy to confirm the XRD data and identify secondary phases.

Figure 7 depicts the Raman spectra of Sb_xSe_y films. All samples are characterized by the presence of peaks corresponding to antimony selenide (80, 151, 185, 189, 210 cm^{-1}), various phases of selenium (102, 129, 234–237, 250 cm^{-1}) and antimony oxide (118–123, 140, 189, 255 cm^{-1}) [20, 21]. Difficulties in finding the presence of the pure antimony phase are created by the fact that the peak of 150 cm^{-1} is characteristic of both antimony and antimony selenide, but the presence of a peak at 110 cm^{-1} suggests that pure antimony is present in all films [22, 23]. The peaks corresponding to different phases of selenium and antimony oxide have a much lower intensity and are not identified in the X-ray diffraction patterns, which may indicate the presence of these phases only on the surface of the films.

The diffraction patterns of the studied samples (Fig. 5) show a redistribution of the intensities of the diffraction lines with a change in the Sb/Se ratio, which indicates a change in the predominant orienta-

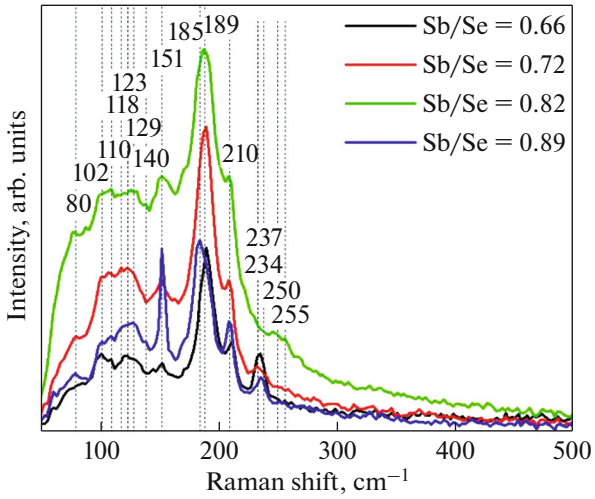

Fig. 7. Raman spectra of Sb_2Se_3 thin films.

tion of the crystallites in the films. It should be noted that the orientation of crystallites is critical to ensure efficient charge transfer in the photoactive layer, since due to Sb_2Se_3 structural features, a strong anisotropy of the electrooptical properties in directions is observed, which ultimately determines the efficiency of solar cells based on Sb_2Se_3 thin films [24].

To assess the predominant orientation of crystallites, the texture coefficient $TK_{(hkl)}$ is commonly used, which is calculated by the formula [25]:

$$TK_{(hkl)} = \frac{\dfrac{I(hkl)}{I_0(hkl)}}{\dfrac{1}{N}\sum_{i=1}^{N}\dfrac{I(h_ik_il_i)}{I_0(h_ik_il_i)}}, \qquad (4)$$

where $I(hkl)$ and $I_0(hkl)$ are the intensities of diffraction lines (hkl) for the synthesized films and reference (JCPDS), correspondingly, N is the number of lines. Figure 8a shows the results of calculations of the texture coefficient; Fig. 8b represents the change in the fraction of crystallites with $hk0$ and $hk1$ orientations in films of various compositions. The synthesized films have different textures, the minimum fraction of crystallites with the $hk1$ orientation (the maximum with the $hk0$ orientation) corresponds to the ratio Sb/Se = 0.82, while approaching the stoichiometric ratio, the fraction of crystallites with the $hk1$ orientation increases, and the fraction of crystallites with the $hk0$ orientation decreases. It worth to note the correlation of the roughness parameters (tab. 1) with the orientation of the crystallites, which changes with the change in the ratio of the components of the obtained films. The minimum detected values of the roughness parameters Sa and Sq correspond to the $hk0$ type orientation, and the maximum values correspond to the $hk1$ type orientation.

It should be noted that by now the highest efficiency of Sb_2Se_3-based solar cells has been achieved for the photoactive layer of a thin film of nanorod array grown in the [001] direction [26]. This is probably due to the structure of Sb_2Se_3 crystals, which consist of ribbon-like $(Sb_4Se_6)_n$ units linked by van der Waals forces in the [010] and [100] directions, while the Sb–Se covalent bonds hold the units in the [001] direction [26, 27]. It has been shown [27] that the longitudinal transport of charge carriers is hindered in Sb_2Se_3 films with predominant diffraction peaks $hk0$, and the longitudinal conductivity sharply increases with an increase in the fraction of crystallites with $hk1$ orientations.

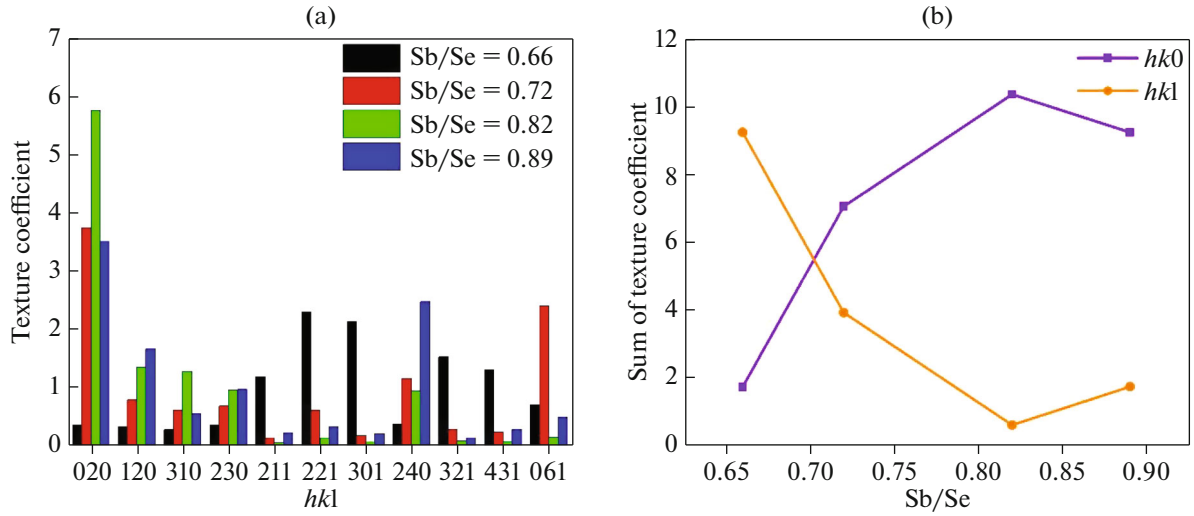

Fig. 8. Histogram of the values of the texture coefficient of thin films Sb_xSe_y (a) and dependence of the fraction of crystallites with orientations $hk0$ and $hk1$ on the ratio Sb/Se (b).

Table 2. Electric parameters of Sb_xSe_y films synthesized with the different ratio Sb/Se

Sb/Se ratio	0.66	0.72	0.82	0.89
*hk*1/*hk*0 ratio	5.88	0.53	0.07	0.16
Resistance (T = 300 K), MOhm	50	54	251	143
Activation energy, eV	0.44	0.43	0.44	0.46

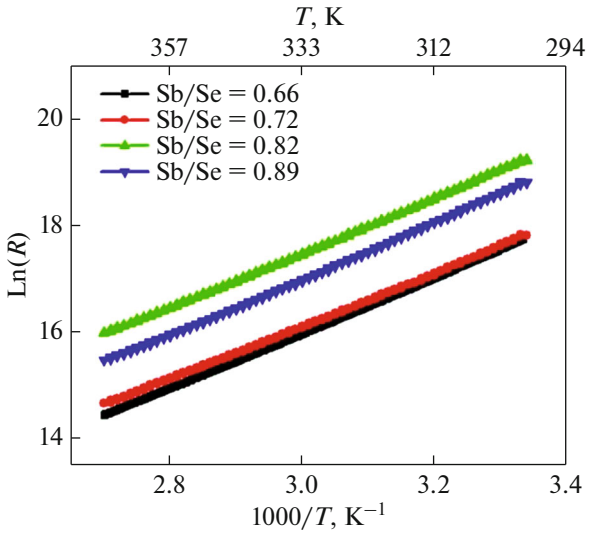

Fig. 9. The dependences of the dark resistance of the Sb_xSe_y samples on temperature.

To examine the influence of the preferred orientation of crystallites on the electrical properties of Sb_xSe_y thin films synthesized by CMBD method, the temperature dependences of the resistance of Sb_xSe_y samples with different Sb/Se ratio were obtained.

Figure 9 shows the dependences of the dark resistance of the Sb_xSe_y samples on temperature in Arrhenius coordinates. As it is seen from Fig. 9, in the studied temperature range an increase in the fraction of crystallites with an orientation of the *hk*1 type (see Fig. 8b) cause the decrease of resistivity of the films.

The linearization of the temperature dependences of the electrical resistance in Arrhenius coordinates indicates an activation mechanism for the generation of charge carriers. The activation energy can be determined according to the well-known formula:

$$E_a = k\frac{\Delta \ln R}{\Delta \frac{1}{T}}, \quad (5)$$

where k is the Boltzmann constant, T and R are the values of temperatures and resistances, respectively.

The activation energy calculated by formula (5) turned out to be in the range of 0.43–0.47 eV for all the studied samples (Table 2). We did not find a pronounced dependence of the activation energy on the preferred orientation of the crystallites in the samples; a small difference between the calculated values of activation energies indicates the same activation mechanism for all films. The resulting activation energy according to [28] can correspond to selenium vacancies. As follows from Table 2, there is a strong correlation between the texture of the synthesized Sb_xSe_y films and their electrical resistance, a change in the relative proportion of crystallites fraction with orientations the *hk*1 and *hk*0 leads to a change in the electrical conductivity of the films. The minimum value of the *hk*1/*hk*0 ratio, which is realized at Sb/Se = 0.82, corresponds to Sb_2Se_3 films with the highest electrical resistance value. The maximum fraction of crystallites with the *hk*1 orientation and the minimum resistance value correspond to a film with a Sb/Se ratio close to stoichiometric. Thus, the CMBD method used makes it possible to create thin Sb_2Se_3 films with the different electrical conductivities, which determines the efficiency of solar cells based on Sb_2Se_3 thin films.

CONCLUSIONS

It has been established that the Sb_xSe_y thin films obtained by CMBD method, having a stoichiometric ratio of components or enriched in antimony, consist of the main Sb_2Se_3 phase which belongs to the orthorhombic syngony. The distribution of Sb and Se over the surface of the synthesized films is uniform for all Sb/Se ratios. While approaching the stoichiometric Sb/Se ratio the values of the roughness parameters Sa and Sq increase, the orientation of microcrystal roads in the film changes from oblique to parallel to the substrate, and the rods themselves become slightly small, their distribution over the substrate becomes even.

Using the advantages of the CMBD method, it is possible to control the composition of Sb_xSe_y thin films, which leads to a change in the texture. The texture of Sb_xSe_y films, in turn, determines their electrical properties. The films obtained with a Sb/Se component ratio close to stoichiometry are characterized by a

predominant *hk*1 orientation of crystallites and lower electrical resistance value. Therefore, the higher efficiency should be expected from photovoltaic modules based on a thin Sb_xSe_y films with a ratio Sb/Se close to stoichiometric.

The possibility of obtaining Sb_xSe_y thin films with the predominant *hk*1 orientations of crystallites by the CMBD method is important for the creation of efficient Sb_2Se_3-based solar cells ensuring efficient charge transfer in the photoactive layer.

FUNDING

This work was supported by the Ministry of innovative development of the Republic of Uzbekistan (Grant no. MRB-2021–540) and the State Committee on Science and Technology of the Republic of Belarus (Grant no. F21UZBG-022).

CONFLICT OF INTEREST

The authors of this work declare that they have no conflicts of interest.

REFERENCES

1. Green, M.A., Dunlop, E.D., Hohl-Ebinger, J., Yoshita, M., Kopidakis, N., and Hao, X., Solar cell efficiency tables (version 60), *Prog. Photovoltaics Res. Appl.,* 2022, vol. 30, pp. 687–701. https://doi.org/10.1002/pip.3595
2. Mavlonov, A., Razykov, T., Raziq, F., et al., A review of Sb_2Se_3 photovoltaic absorber materials and thin-film solar cells, *Sol. Energy,* 2020, vol. 201, pp. 227–246.
3. Jun Wang, Kanghua Li, Jiang Tang, and Chao Chen, A perspective of antimony chalcogenide photovoltaics toward commercialization, *Sol. RRL,* 2023, vol. 7, no. 17, p. 2300436.
4. Xinsheng Liu, Jie Chen, and Miao Luo, Thermal evaporation and characterization of Sb_2Se_3 thin film for substrate Sb_2Se_3/CdS solar cells, *Appl. Mater. Interfaces,* 2014, vol. 6, pp. 10687–10695.
5. Li, Z., Zhu, H., Guo, Y., Niu, X., Chen, X., Zhang, C., Zhang, W., Liang, X., Zhou, D., and Chen, J., Efficiency enhancement of Sb_2Se_3 thin-film solar cells by the co-evaporation of Se and Sb_2Se_3, *Appl. Phys Express,* 2016, vol. 9, no. 5, p. 052302.
6. Wang, L., Li, D.-B., Li, K., Chen, C., et al., Stable 6%-efficient Sb_2Se_3 solar cells with a ZnO buffer layer, *Nat. Energy,* 2017, vol. 2, no. 4, p. 17046.
7. Liang, G.-X., Zhang, X.-H., Ma, H.-L., et al., Facile preparation and enhanced photoelectrical performance of Sb_2Se_3 nanorods by magnetron sputtering deposition, *Sol. Energy Mater. Sol. Cells,* 2017, vol. 160, pp. 257–262.
8. Hutter, O.S., Phillips, L.J., Yates, P.J., et al., CSS Antimony selenide film morphology and high efficiency PV devices, in *2018 IEEE 7th World Conference on Photovoltaic Energy Conversion (WCPEC) (A Joint Conference of 45th IEEE PVSC, 28th PVSEC & 34th EU PVSEC),* IEEE, pp. 0027–0031.
9. Kwon, Y.H., Kim, Y.B., Jeong, M. et al., Crystal growth direction-controlled antimony selenide thin film absorbers produced using an electrochemical approach and intermediate thermal treatment, *Sol. Energy Mater. Sol. Cells,* 2017, vol. 172, pp. 11–17.
10. Zhou, Y., Leng, M., Xia, Z., Zhong, J., Song, H., Liu, X., Yang, B., Zhang, J., Chen, J., Zhou, K., Han, J., Cheng, Y., and Tang, J., Solution-processed antimony selenide heterojunction solar cells, *Adv. Energy Mater.,* 2014, vol. 4, p. 1301846.
11. Khan, M.D., et al., Novel single source precursor for synthesis of Sb_2Se_3 nanorods and deposition of thin films by AACVD: Photo-electrochemical study for water reduction catalysis, *Sol. Energy,* 2018, vol. 169, pp. 526–534. https://doi.org/10.1016/j.solener.2018.05.026
12. Wen, X., et al., Vapor transport deposition of antimony selenide thin film solar cells with 7.6% efficiency, *Nat. Commun.,* 2018, vol. 9, no. 1, p. 2179. https://doi.org/10.1038/s41467-018-04634-6
13. Razykov, T.M., Chemical molecular beam deposition of II–VI binary and ternary compound films in a gas flow, *Appl. Surf. Sci.,* 1991, vol. 48, pp. 89–92.
14. Razykov, T.M., Shukurov, A.Kh., Kuchkarov, K.M., et al., Morphological and structural characteristics of Sb_2Se_3 thin films fabricated by chemical molecular beam deposition, *Appl. Sol. Energy,* 2019, vol. 55, pp. 376–379.
15. Razykov, T.M., Kuchkarov, K.M., Ergashev, B.A., Tursunkulov, O.M., Olimov, A., Isakov, D., Makhmudov, M., and Pirimmatov, M., Microstructural, Optical, and electrical properties of Sb_2Se_3 films fabricated by the CMBD method for solar cells, *Appl. Sol. Energy,* 2022, vol. 58, no. 1, pp. 21–27.
16. Ghosh, G., The Sb-Se (antimony-selenium) system, *J. Phase Equilibria,* 1993, vol. 14, no. 6, pp. 753–763.
17. Vidal-Fuentes, P., et al., Multiwavelength excitation Raman scattering study of Sb_2Se_3 compound: Fundamental vibrational properties and secondary phases detection, *2D Mater.,* 2019, vol. 6, no. 4, p. 45054.
18. Shongalova, A., Correia, M.R., Vermang, B., V Cunha, J.M., Salomé, P.M.P., and Fernandes, P.A., On the identification of Sb_2Se_3 using Raman scattering, *MRS Commun.,* 2018, vol. 8, no. 3, pp. 865–870.
19. Sui, Z., et al., Laser effects on phase transition for cubic Sb_2O_3 microcrystals under high pressure, *J. Mater. Chem. C,* 2017, vol. 5, no. 22, pp. 5451–5457.
20. Nagata, K., Ishibashi, K., and Miyamoto, Y., Raman and infrared spectra of rhombohedral selenium, *Jpn. J. Appl. Phys.,* 1981, vol. 20, no. 3, p. 463.
21. Mestl, G., Ruiz, P., Delmon, B., and Knozinger, H., Sb_2O_3/Sb_2O_4 in reducing/oxidizing environments: An in situ Raman spectroscopy study, *J. Phys. Chem.,* 1994, vol. 98, no. 44, pp. 11276–11282.
22. Li, Z., et al., Sb_2Se_3 thin film solar cells in substrate configuration and the back contact selenization, *Sol. Energy Mater. Sol. Cells,* 2017, vol. 161, pp. 190–196.
23. Zhou, Y., et al., Solution-processed antimony selenide heterojunction solar cells, *Adv. Energy Mater.,* 2014, vol. 4, no. 8, p. 1301846. https://doi.org/10.1002/aenm.201301846

24. Ying Zhou, Liang Wang, Shiyou Chen, et al., Thin-film Sb_2Se_3 photovoltaics with oriented one-dimensional ribbons and benign grain boundaries, *Nat. Photonics,* 2015, vol. 9, no. 6, pp. 409–415.

25. Li, Z., Chen, X., Zhu, H., Chen, J., Guo, Y., Zhang, C., Zhang, W., Niu, X., and Mai, Y., Sb_2Se_3 thin film solar cells in substrate configuration and the back contact selenization, *Sol. Energy Mater. Sol. Cells,* 2017, vol. 161, pp. 190–196. https://doi.org/10.1016/j.solmat.2016.11.033

26. Wang, D., Song, C., Fu, X., and Li, X., Growth of one-dimensional Sb_2S_3 and Sb_2Se_3 crystals with straw-tied-like architectures, *J. Cryst. Growth,* 2005, vol. 281, pp. 611–615.

27. Deringer, V.L., Stoffel, R.P., Wuttig, M., and Dronskowski, R., Vibrational properties and bonding nature of Sb_2Se_3 and their implications for chalcogenide materials, *Chem. Sci.,* 2015, vol. 6, pp. 5255–5262.

28. Jiabin Dong, Yue Liu, Zuoyun Wang., et al., Boosting VOC of antimony chalcogenide solar cells: A review on interfaces and defects, *Nano Select.,* 2021, vol. 2, no. 10, pp. 1818–1848.